Key Points:
- The probability of occurrence of stagnation zones and reverse flow is computed based on the uncertainty caused by river boundary conditions
- Polynomial chaos expansions are used in an element-wise fashion for quantifying the propagation of uncertainty
- The regions near the confluence of two streams are very dynamic and prone to the presence of stagnation points and reverse flow

Correspondence to:
G. Chiogna,
gabriele.chiogna@tum.de

Author Contributions:
Conceptualization: P. Merchán-Rivera, B. Wohlmuth, G. Chiogna
Data curation: P. Merchán-Rivera
Formal analysis: P. Merchán-Rivera, B. Wohlmuth, G. Chiogna

Identifying Stagnation Zones and Reverse Flow Caused by River-Aquifer Interaction: An Approach Based on Polynomial Chaos Expansions

P. Merchán-Rivera[1] ⓘ, B. Wohlmuth[2,3], and G. Chiogna[1,4] ⓘ

[1]Hydrology and River Basin Management, Technical University of Munich, Munich, Germany, [2]Numerical Mathematics, Technical University of Munich, Munich, Germany, [3]Department of Mathematics, University of Bergen, Bergen, Norway, [4]Institute of Geography, University of Innsbruck, Innsbruck, Austria

Abstract Fluctuating stream stages and peak-flow events can significantly influence the interactions between streams and aquifers and modify the hydraulic gradient, the flux exchange and the subsurface flow paths. As a result, stagnation zones and reverse flow may appear in different parts of an aquifer and at different times. These features of the flow field play a relevant role in the transport, transformation, and residence time of solutes, pollutants, and nutrients in the subsurface. However, their identification using numerical models is complex not only because of highly nonlinear dynamics, but also due to significant uncertainties in the model input data which propagate into the quantities of interest. In this work, we use an approach based on polynomial chaos expansions to map the probability of occurrence of stagnation zones and reverse flow during a flood event. We quantify the propagation of uncertainty into the groundwater flow field due to the applied river boundary conditions. Then, we evaluate the responses of the posterior probabilities in an element-wise fashion using a set of flow classification criteria and kernel density estimations. The proposed methodology is flexible because it employs a nonintrusive pseudo-spectral technique and, consequently, it can be applied straightforwardly in preexisting models. The regions near the confluence of two streams in the studied area are prone to present transient stagnation and reverse flow.

1. Introduction

There is a long-standing scientific awareness of the importance of the interactions between streams and aquifers (Brunner et al., 2017; Krause et al., 2014; Lewandowski et al., 2019, 2020; Magliozzi et al., 2018; Stanford & Ward, 1988; Winter, 1998, 1999). Many investigations describe the role of the dynamics of these interactions in the transport, degradation, and residence time of solutes and pollutants (Boano et al., 2014; Elliott & Brooks, 1997; Singh et al., 2020; Trauth & Fleckenstein, 2017), the transport of nutrients, the ecosystem metabolism and the biogeochemical transformations at the interface (Boano et al., 2014; Findlay, 1995; Jones & Holmes, 1996; Pinay et al., 2015), as well as the modulation of temperature (Arrigoni et al., 2008; Bhaskar et al., 2012; Gerecht et al., 2011; Marzadri et al., 2013). Mass and energy exchange are defined by the distribution of the hydraulic heads, the flow path directions, the canal bed conditions and the stream hydraulics (Lewandowski et al., 2019; Woessner, 2000). Thus, the stream-aquifer interaction (i.e., river-aquifer interaction) is a function of space and time that may vary not only due to the geomorphologic and hydrogeologic controls, but also due to the occurrence, magnitude, and distribution of hydrologic conditions (e.g., flood events) and anthropogenic impacts (e.g., hydropeaking). Numerous studies have also reported that rapid and fluctuating stages and peak-flow events can significantly affect the stream-aquifer interaction and modify the water flux, the residence times, and the flow paths in the subsurface flow (Bernard-Jannin et al., 2016; Boano et al., 2013; Cardenas, 2008; Casas-Mulet et al., 2015; Malzone et al., 2016; Singh et al., 2020; Trauth & Fleckenstein, 2017; Wu et al., 2018). Still, as recognized by Conant et al. (2019) and Krause et al. (2017, 2014), we need to develop new methods to describe the stream-aquifer dynamics in spatial and temporal terms to advance in the mechanistic understanding and predictability of these systems.

Irregular flow paths may affect fluid mixing and transport (Zhang et al., 2009) and consequently, reactive solute transport in geophysical flows (Chiogna et al., 2012; Sund et al., 2015). For instance, fluctuating head gradients change the rates of the groundwater flow and can create stagnation zones (Anderson & Munter, 1981; Cardenas, 2008; Tóth, 1963; Winter, 1976), regions associated with stagnation or equilibrium points (Jiang

et al., 2011), where the groundwater velocity is zero (Bear, 1972). Nontrivial flow patterns can be observed near the stagnation points, which are relevant to the identification of the origin and fate of fluids and solutes (Bresciani et al., 2019). These points can allocate mixing and highly reactive regions, control the behavior of dissolution, dissipation, and reaction rates (Hidalgo & Dentz, 2018; Hidalgo et al., 2015; Jiang et al., 2014), and promote biogeochemical transformations (Krause et al., 2014; Pinay et al., 2015; Singh et al., 2020). Moreover, the location of stagnation points supports the description of the groundwater flow patterns in regimes that are driven by topographical and morphological configurations (Gomez & Wilson, 2013; Jiang et al., 2011; Ren & Zhao, 2020; Wang et al., 2017). Additionally, transient stages in the stream-aquifer interactions can be relevant to the evaluation of multidirectional variations in the flow field. The rise of stream stages may reverse the dominant direction of the groundwater flow regime (Hunt et al., 2006) and affect the circulation of nutrients and solutes (Dudley-Southern & Binley, 2015). Additionally, the reversals in the hydraulic gradient can switch between losing and gaining stream conditions, and influence the infiltration depth of solutes and the reaction rates in the subsurface (Trauth & Fleckenstein, 2017).

Groundwater numerical models are frequently used to understand stream-aquifer interactions (Anderson et al., 2015; Peyrard et al., 2008). Major uncertainties may propagate into the model outcomes due to the error in the observed hydrological variables, the parameterization and structure of the model, as well as the conceptual assumptions and simplifications (Brunner et al., 2010; Di Baldassarre & Montanari, 2009; Götzinger & Bárdossy, 2008). In the field of hydrology, the propagation of the uncertainty has often been quantified by implementing Monte Carlo methods and related ensemble techniques (Beven & Binley, 1992; Kuczera & Mroczkowski, 1998; Vrugt et al., 2003). The main drawbacks of these approaches are typically the high number of simulations to cover the stochastic space of the uncertain parameters accordingly (Cools & Nuyens, 2016). Spectral expansion methods, such as generalized polynomial chaos (gPC), are suitable options to tackle these issues, particularly, to solve low-dimensional stochastic problems (Le Maitre & Knio, 2010; Smith, 2013). By using gPC expansions, we can represent different stochastic processes based on a suitable orthogonal polynomial basis (Rajabi, 2019; Xiu, 2009; Xiu & Karniadakis, 2002) and represent the full randomness of the system responses with expansion coefficients (Rajabi et al., 2015).

Previous investigations have properly implemented polynomial expansion methods to solve simplified analytical problems associated with hydrology, hydrogeology, and hydraulics (Esfandiar et al., 2015; Francis et al., 2010; Gibson et al., 2014; Litvinenko et al., 2020; Maina & Guadagnini, 2018; Meng & Li, 2017; Oladyshkin et al., 2012; Rajabi, 2019; Sochala & Le Maître, 2013; Zhang & Lu, 2004). Yet, the application of polynomial expansion techniques in hydrological field studies have received less attention (Deman et al., 2016; Ghaith & Li, 2020; Laloy et al., 2013; Rajabi & Ataie-Ashtiani, 2016). In addition, evaluation of the polynomial expansions performance in groundwater applications is still an open matter (Rajabi, 2019), and its application for the quantification of the uncertainty caused by stream-aquifer interactions remains unexplored. In fact, the efficiency of spectral methods is problem-dependent (Le Gratiet et al., 2017). Therefore, to benefit from the application of these tools and to produce appropriate conclusions, we need to examine a large number of hydrological case studies.

This work aims to map the occurrence of complex flow processes caused by stream-aquifer interactions in terms of temporal dynamics and spatial patterns. By exploiting the strengths of gPC expansions, we want to distinguish reverse flow and stagnation hotspots and describe them in terms of probability of occurrence. We use gPC expansions to quantify the propagation of uncertainty in the groundwater flow field due to the uncertain river boundary conditions during a flood event. We define the evaluation criteria to classify flow types and explore the posterior probabilities in an element-wise fashion (i.e., cell-by-cell) of a distributed model using kernel density estimations. The approach that we propose aims to assess the randomness of the input uncertainty of parameters that are variable in time and hence are commonly unknown in the parameterization of stream-aquifer relations, such as the streambed conductance and the stream stages. These parameters are often used to fine-tune, recalibrate, and update the hydrogeologic models. Then, hydraulic conductivity, specific storage, specific yield, and effective porosity are excluded from our set of stochastic parameters. Even if these aquifer properties are uncertain and can be evaluated using gPC theory, once a numerical model is developed, they are assumed as constant input parameters over time (Bachmat et al., 1978; Osman, 2013). On the other hand, variation of the streambed conductance as a function of time has been largely reported (Cui et al., 2020; Hatch et al., 2010; Hubbs, 2006; Stewardson et al., 2016), and the stream stage is, by definition, a fluctuating attribute of the streamflow (Reddy, 2005). Furthermore, by using pseudo-spectral expansions, the groundwater model does not require to be modified and can

be treated as a black box in the computational procedure. Hence, this method can be applied to preexisting models where the spatial and temporal implications of the stream-aquifer interactions play a relevant role.

2. Methods

2.1. Groundwater Flow and River Boundary Conditions

Transient groundwater flow in a heterogeneous unconfined aquifer, when the coordinate system is oriented parallel to the major axes of anisotropy, can be expressed by a partial differential equation (Fetter, 1999):

$$\frac{\partial}{\partial x}\left(k_{xx}\frac{\partial h}{\partial x}\right) + \frac{\partial}{\partial y}\left(k_{yy}\frac{\partial h}{\partial y}\right) + \frac{\partial}{\partial z}\left(k_{zz}\frac{\partial h}{\partial z}\right) + W = S_s\frac{\partial h}{\partial t}, \tag{1}$$

where h is the piezometric head [L], k_{xx}, k_{yy}, and k_{zz} represent the hydraulic conductivity along the x, y, and z coordinate axes [LT^{-1}], S_s is the specific storage [L^{-1}], and W is the volumetric flux per unit volume to represent the sources and sinks [T^{-1}]. For practical applications, Equation 1 is often solved by numerical methods as a set of spatially discrete points in the center of a cell. So, the rate of change in storage within each cell is equal to the sum of flows into and out of the cell, as follows (Harbaugh, 2005):

$$\sum Q_i = S_s\frac{\Delta h}{\Delta t}\Delta V, \tag{2}$$

where Q_i is the i component of the flow rate into the cell that includes the source and sink terms [L^{3}T^{-1}], ΔV is the cell volume [L^3], and Δh [L] is the change in the groundwater head over a time interval Δt [T]. External sources or stressors (e.g., rivers, artificial waterways, and lakes) can be represented as Q_i elements to predict head distributions at successive times for transient simulations. The interaction between surface water and groundwater is frequently conceptualized as a boundary condition for the head-dependent flux (Anderson et al., 2015; Brunner et al., 2010; Di Ciacca et al., 2019). Hence, the flux exchange between streams and aquifers, Q_e, is represented as follows:

$$Q_e = \begin{cases} c_r(h_r - b_r), & h_a \le b_r \\ c_r(h_r - h_a), & h_a > b_r \end{cases}, \tag{3}$$

where c_r is the streambed conductance [L^{2}T^{-1}], h_r is the water level or stream stage [L], b_r is the bottom of the streambed [L], and h_a represents the hydraulic head at the node in the cell underlying the stream reach [L]. The term c_r in the river package of MODFLOW-2005 is a resistance factor defined by the stream width w_r [L], the length of the conductance block l_r [L], the thickness of the streambed m_r [L], and the vertical hydraulic conductivity of the streambed material k_r [LT^{-1}] (Harbaugh, 2005):

$$c_r = \frac{k_r l_r w_r}{m_r}. \tag{4}$$

Streambed conductance is a broadly applied approach in hydrogeologic modeling (Morel-Seytoux, 2019). Nonetheless, it is a very simplified conceptualization of the stream-aquifer interactions that assumes homogeneity and isotropy of the streambed hydraulic conductivity within the cell (Cardenas & Zlotnik, 2003; Ghysels et al., 2018, 2019). Furthermore, the river package is not able to represent flow in the unsaturated zone (Brunner et al., 2010; Ghysels et al., 2019). In our application, the unsaturated flow under the stream can be neglected due to the active hydraulic connection during the simulated period. On the other hand, major roles are played by c_r and h_r, and they are included in the uncertainty analysis accordingly. Overall, these parameters can show large spatial and temporal variability, and they are frequently uncertain, hardly accessible, or even unknown. In practice, c_r is a lumped parameter that cannot be easily measured in the field, that comprises various properties of the streambed (Cousquer et al., 2017; Mehl & Hill, 2010), and that is often estimated by calibration (Morel-Seytoux et al., 2017). The uncertainty in the estimation of h_r originates from the stream flow data (Di Baldassarre & Montanari, 2009) and the model structure (Georgakakos et al., 2004).

To define the velocity distribution, transient simulations can be represented as a series of discrete steady-state flow periods (Pollock, 2012). The stationary version of Equation 1 can be rewritten in terms of the average linear groundwater velocity as:

$$\frac{\partial}{\partial x}(\eta v_x) + \frac{\partial}{\partial y}(\eta v_y) + \frac{\partial}{\partial z}(\eta v_z) = W,$$
(5)

where v_x, v_y, and v_z represent the principal components of the averaged linear velocity [L/T], and η is the effective porosity [-]. Then, to obtain the averaged linear velocity component across one face of the cell, we can represent the volumetric flow rates across the finite-sized cell within a structured aligned grid in this fashion:

$$\frac{(\eta v_{x_2} - \eta v_{x_1})}{\Delta x} + \frac{(\eta v_{y_2} - \eta v_{y_1})}{\Delta y} + \frac{(\eta v_{z_2} - \eta v_{z_1})}{\Delta z} = \frac{Q_s}{\Delta x \; \Delta y \; \Delta z} \; .$$
(6)

Equation 6 is formed by Q_s as the internal sources or sinks within the cell, Δx, Δy, and Δz as the dimensions of the cell in the respective coordinate directions, and the components v_{x_1}, v_{x_2}, v_{y_1}, v_{y_2}, v_{z_1}, and v_{z_2} that represent the velocities perpendicular to the respective coordinate direction at the six faces of the cell. Equation 6 can be solved using the values of the groundwater heads Δh at a given distance Δl [L] by substituting each of the flow terms by Darcy's law. For instance, Equation 7 exemplifies the definition of the velocity perpendicular to the x-direction at one face (Pollock, 2012):

$$v_{x_1} = \frac{Q_{x_1}}{\eta \Delta y \Delta z} = \frac{-k_{xx}\Delta h_{x_1}}{\eta \Delta l_{x_1}}.$$
(7)

2.2. Polynomial Chaos Expansion and Pseudo-Spectral Approach

Within the context of uncertainty quantification, generalized Polynomial chaos theory (Xiu & Karniadakis, 2002) refers to the representation of random spaces by spectral expansions (Smith, 2013; Xiu, 2009). Following the generalized Cameron-Martin theorem (Cameron & Martin, 1947), we define a second-order random (finite variance) process (Smith, 2013) by a general polynomial approximation:

$$f(s, t; \Phi) = \sum_{i=0}^{\infty} \hat{c}_i(s, t)\Psi_i(\Phi),$$
(8)

where $f(s, t; \Phi)$ is the output function defined by both the deterministic spatio-temporal dependencies $\{s, t\}$, and the stochastic dependencies $\Phi = (\varphi_1, \ldots, \varphi_d)$, $\hat{c}_i(s, t)$ are deterministic coefficients, and $\Psi_i(\Phi)$ are orthogonal polynomials that form the basis for the stochastic component of the solution. The random events Φ represent the stochasticity in the system due to uncertain parameters, source terms, initial or boundary conditions, etc. For the case of this study, this is the uncertainty related to the parameterization of the river boundary conditions: c_r and h_r. In practice, the series in Equation 8 must be truncated after N terms, to obtain a finite approximation:

$$f(s, t; \Phi) \approx \sum_{i=0}^{N} \hat{c}_i(s, t)\Psi_i(\Phi).$$
(9)

In Equations 8 and 9, we observe that the polynomial approximation separates the deterministic and the stochastic components. The polynomial basis functions $\Psi_i(\Phi)$ must be properly specified according to the probability density function of the random variables (Xiu & Karniadakis, 2002). The basis construction of a single random variable $\psi_i(\varphi)$ will satisfy the orthogonality condition with respect to the density $\rho_\Phi(\varphi)$, such that:

$$\mathbb{E}[\psi_i(\Phi)\psi_j(\Phi)] = \int_\Gamma \psi_i(\varphi)\psi_j(\varphi)\rho_\Phi(\varphi)d\varphi = \langle \psi_i, \psi_j \rangle_\rho = \gamma_i \delta_{ij},$$
(10)

where $\langle \psi_i, \psi_j \rangle_\rho$ is the inner product of ψ_i and ψ_j on the interval Γ with the weighting function $\rho_\Phi(\varphi)$, $\gamma_i = \mathbb{E}[\psi_i^2(\Phi)] = \langle \psi_i \rangle^2$ is a normalization factor, and δ_{ij} denotes the Kronecker delta. As described later in Section 4.5, to construct the orthogonal polynomials in this study, the uniform distributions of the river and canal

conductance lead to the Legendre-chaos polynomials, while the Hermite-chaos polynomials correspond to normal distribution of the stream stages.

As stated by Smith (2013), the representation of random processes that are functions of d multiple independent random variables is analogous to the univariate case and the multidimensional basis can be constructed as tensor products of univariate polynomials. Since the underlying $\Psi_i(\Phi)$ in Equation 9 are known and previously defined, we only need to compute $\hat{c}_i(s, t)$ to obtain the gPC expansion. In this work, we apply a nonintrusive expansion known as the pseudo-spectral approach (Xiu, 2007). We use this method because it applies a set of deterministic model resolutions using specific realizations of Φ to construct approximations (Le Maitre & Knio, 2010). Therefore, we can treat the solver as a black box in the computational procedure. This process requires numerical integration. In this work, we use an optimal Gaussian quadrature (Gautschi, 1968; Golub & Welsch, 1968) over a full tensor product of integration order K to achieve order n polynomials. This specifies a set of Gaussian quadrature nodes $q_k = (q_1, \ldots, q_K)$ and weights $w_k = (w_1, \ldots, w_K)$, following the method defined by Gautschi (1968). Then, the number of model evaluations P is equal to $(K + 1)^d$. The calculation of $\hat{c}_i(s, t)$ then follows:

$$\hat{c}_i(s, t) = \langle f(s, t, \varphi), \psi_i(\varphi) \rangle_\rho = \int_\Gamma f(s, t, \varphi) \psi_i(\varphi) \rho_\Phi(\varphi) d\varphi, \tag{11}$$

$$\hat{c}_i(s, t) \approx \sum_{k=0}^{K} f(s, t, q_k) \psi_i(q_k) w_k. \tag{12}$$

The number of nodes K can be defined by $(n + d)!/n!d! - 1$ (Smith, 2013; Xiu, 2010) to represent the n interaction terms optimally, or by using experimental combinations such as the empirical rule $K = (d - 1)N$, where $N = n + 1$ (Sudret, 2008). Once the forward deterministic evaluations are run and $\hat{c}_i(s, t)$ are approximated, we can compute the polynomial expansions $f(s, t; \Phi)$. We can also straightforwardly obtain the first and second statistical moments by the following equations:

$$\mathbb{E}[f(s, t; \Phi)] = \mu_f = \hat{c}_0(s, t), \tag{13}$$

$$\mathbb{V}[f(s, t; \Phi)] = \sigma_f^2 = \sum_{k=1}^{K} \hat{c}_k^2(s, t). \tag{14}$$

2.3. Kernel Density Estimation

The statistics of the quantity of interest, μ_f (expected value) and σ_f (standard deviation), are point estimates because they represent a single value in the parameter space. However, for understanding the uncertainty and extending the analysis to the spatial and temporal variations, computing the underlying probability density function may be quite informative, and also practical to estimate the probability of occurrence of stagnation points and reverse flow. We apply a nonparametric estimation technique known as kernel density estimation (Silverman, 1998; Wand & Jones, 1995). This method calculates the density function by weighting the distances of the realizations from a point x. The kernel estimator $\hat{f}(x)$ is defined by:

$$\hat{f}(x) = \frac{1}{nb_\xi} \sum_{i=1}^{n} \xi\left(\frac{x - X_i}{b_\xi}\right). \tag{15}$$

where X_i are independent data points drawn from the actual gPC expansions, b_ξ is the window width or bandwidth, ξ is the window function that determines the shape of the kernel, and n is the sample size. For this study, b_ξ is defined following Scott's Rule as $b_\xi \equiv 3.5\sigma n^{-1/3}$ (Scott, 2014), and κ is a Gaussian kernel defined as:

$$\kappa(x, b_\xi) \propto e^{-\frac{x^2}{2b_\xi^2}}. \tag{16}$$

Once we define the quadrature degree K that is able to represent the randomness of the uncertain inputs at a low computational cost and with a small error in relation to the observed heads, we replicate the method in an
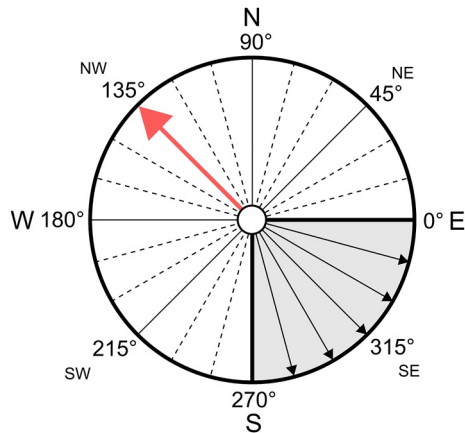
Figure 1. Reverse flow criteria representation: the red arrow represents the reference flow direction before a flood event, the gray area represents the interval within which the directions are considered reversal flows.

element-wise operation to find $\hat{f}(x)$ and obtain the point estimates and posterior probability distributions for each cell of the domain.

2.4. Flow Criteria Classification

The posterior probability distributions can be evaluated according to a set of criteria that reflect the occurrence of particular flow types (i.e., stagnation points and flow reversal) at different phases of the event. The first criterion states the probability of finding stagnation cells, which are cells where the local magnitude of the flow field can be equal to zero. We can explain this condition by defining the cumulative distribution function $\hat{F}_V(v)$ from the previous kernel estimator, as follows:

$$\hat{F}_V(v) = P(V \le v),\tag{17}$$

where the right-hand side is the probability that the magnitude of the flow field V takes on a value less than or equal to v. Then, the probability of finding stagnation cells can be written as:

$$P(V = 0) = \hat{F}_V(0).\tag{18}$$

To identify the probability of occurrence of reverse flow, we need to define a flow field direction of reference with an angle $\bar{\theta}$. Based on this reference direction, we define a flow as reverse when the angle of the evaluated flow direction θ is within the interval $[\alpha, \beta]$, where:

$$\alpha = \bar{\theta} - 135°, \quad \beta = \bar{\theta} + 135°.\tag{19}$$

Figure 1 shows an example of these criteria for a hypothetical reference direction with an angle $\bar{\theta} = 135°$ (red arrow), which means that the flow runs from southeast to northwest. We assume a flow reversal when the angle θ varies between $\alpha = 0°$ and $\beta = 270°$ (gray area), because the flow is no longer flowing to the north nor to the west. In practice, we need to find the angles of the reference directions for every cell in order to map the probability. Notice that the reference flow field direction can be adapted to the requirements of the study, the temporal span and discretization of interest, and the hydraulic responses of the system. For instance, in this study, we use the mean as measurement of central tendency to define $\bar{\theta}$:

$$\bar{\theta} = \frac{1}{n_s} \sum_{i=t_s}^{t_f} \mu_{\theta_i}, \quad n_s = 1 + (t_f - t_s),\tag{20}$$

with μ_{θ_i} representing the expected values of the flow field angle computed with the polynomial expansions, with t_s and t_f representing the first and last stress periods between two flood events or, in our study, the beginning of the simulation and the flood event, and with n_s denoting the number of stress periods between t_s and t_f. Finally, we can define the probability of finding reverse flow and express it in terms of a cumulative density function:

$$P(\alpha \le \theta \le \beta) = \begin{cases} \hat{F}_\theta(\alpha) - \hat{F}_\theta(\beta), \alpha > \beta \\ \\ \hat{F}_\theta(\alpha) + (1 - \hat{F}_\theta(\beta)), \quad \alpha < \beta \end{cases}.\tag{21}$$

2.5. Case Study and Algorithm Implementation

We applied the exposed approach to a real case model. The study area is in the Alz valley in Tacherting, Germany. Figure 2a shows the site location and the schematics of the numerical model. The Alz river flows from south to north along the valley. We can also observe an artificial waterway, the Alz canal, that acts as a tributary of the river. The river and the canal are hydraulically connected to an unconsolidated shallow sedimentary aquifer
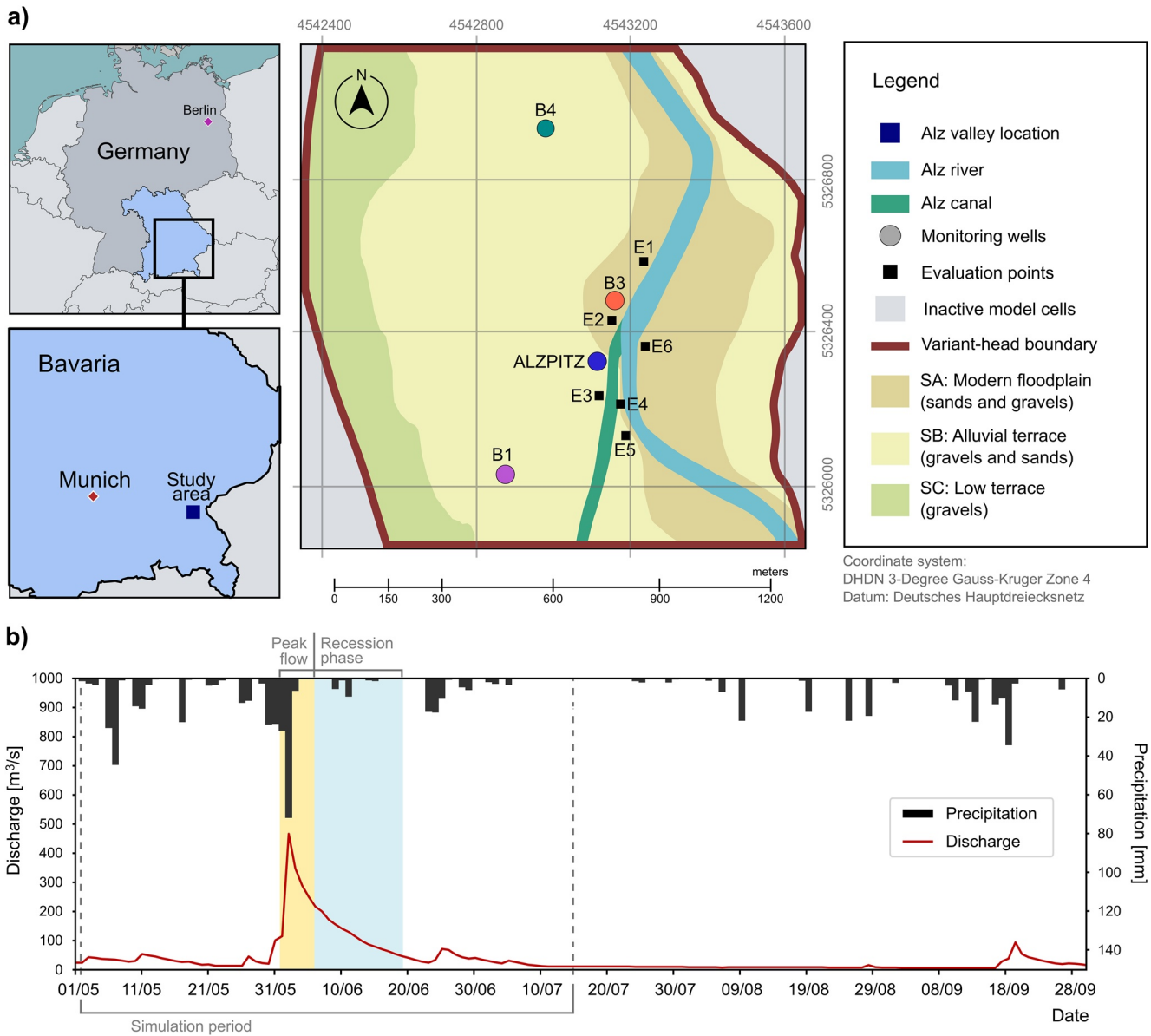
Figure 2. Flood event in 2013 in the Alz valley description: (a) study area location and numerical model settings, and (b) measured discharge in the river Alz and precipitation rate.

(Keilholz et al., 2015; Merchán-Rivera et al., 2018). The bottom of the aquifer is located at 430 m a.s.l (above sea level) and it has an average depth of ~30 m (Doppler et al., 2011). As shown in Figure 2b, the region was affected by a flood event due to heavy rainfall events at the beginning of June 2013.

To describe the interaction between the streams and the aquifer, we built a groundwater numerical model using MODFLOW-2005 (Harbaugh, 2005). This model is based on the model presented in Merchán-Rivera et al. (2018) and the data collected in Keilholz et al. (2015). The spatial domain of the model is subdivided into a finite-difference grid formed by one layer (vertical representation), 260 rows, and 260 columns (horizontal representation). The simulation period covers 75 days from 02 May 2013 00:00:00 to 15 July 2013 18:00:00, and it is discretized in 300 stress periods of 6 h intervals. The number of stress periods used to define n_s is equal to 100 (from 02 May 2013 to 26 May 2013). The aquifer properties of the model were defined according to the underlying geological features presented in previous studies (Bayerisches Landesamt für Umwelt, 2017; Doppler et al., 2011). These studies identified three main soil types in the area: a younger floodplain underneath the Alz river formed by

Table 1
Model Parameters: (a) Deterministic Hydraulic Parameters and (b) Stochastic Stream Parameters

Model parameters	Value	Unit
(a) Deterministic parameters		
Hydraulic conductivity SA	$7.0131e^{-03}$	m/s
Hydraulic conductivity SB	$1.0617e^{-03}$	m/s
Hydraulic conductivity SC	$1.3068e^{-04}$	m/s
Specific storage SA	$2.2475e^{-05}$	1/m
Specific storage SB	$1.9938e^{-06}$	1/m
Specific storage SC	$2.8263e^{-05}$	1/m
Specific yield SA	$1.6561e^{-01}$	–
Specific yield SB	$1.6057e^{-01}$	–
Specific yield SC	$2.0543e^{-01}$	–
Effective porosity	0.3500	–
(b) Stochastic parameters		
Stream stage error	Normal $\sim \mathcal{N}(0, \ 0.145)$	m
Conductance of the river	Uniform $\sim \mathcal{U}(1e^{-7}, 9e^{-4})$	m²/s
Conductance of the canal	Uniform $\sim \mathcal{U}(1e^{-5}, 9e^{-1})$	m²/s

gravel and sand (SA), an alluvial terrace formed by gravel and sand (SB), and a low terrace mainly formed by gravel (SC) (Figure 2a). The soil properties allow a very dynamic behavior of the groundwater flow due to the high permeability of the porous media, the good hydraulic connection with the adjacent streams, and the relatively high rainfall recharge. The hydraulic conductivity, the specific storage, the specific yield of the three soil types and the effective porosity are not considered calibration parameters in this study, since we are using a model that has already been calibrated, and we do not consider these parameters as time dependent. The groundwater responses are field measurements that were registered every 6 h in four groundwater monitoring wells: Alzpitz, B1, B3, and B4 (Keilholz et al., 2015). The hydraulic conductivity, specific storage, specific yield, and effective porosity for each soil zone were calibrated in previous studies (Keilholz et al., 2015; Merchán-Rivera et al., 2018) and are based on the soil properties (Bayerisches Landesamt für Umwelt, 2017; Doppler et al., 2011). Table 1a summarizes the parameterization of the numerical model.

Three boundary conditions were imposed in the model. First, time-variant specified-heads (CHD) were used to simulate the variation in the water table at the borders of the domain. By applying this option, transient heads were adjusted at every stress period. Second, we included recharge into the saturated zone to simulate the distributed flux from the top of the domain due to infiltration. Third, we used the river package (Harbaugh, 2005), the streambed conductance and hydraulic head in the stream to simulate the interaction between surface water and the aquifer. A regional hydrologic model built in MIKE SHE (DHI, 2013) by Keilholz et al. (2015) was used to obtain the scatter stage information for the river and the canal, the recharge into the saturated zone, and the groundwater heads to define the time-variant specified-heads, which change in time and space.

The uncertainty in the river boundary conditions is introduced by the experimental error in the stream stage ε and the streambed conductance c_r, which are assumed to be random variables. The uncertainty related to stream discharges of the region have been previously quantified by Willems (2011) and Willems and Stricker (2012). These works extensively study the uncertainty in the physical measurements of the rivers of the region and describe a normal distribution for the uncertainty in the discharges and the head measurements of the river Alz. This choice considers that the normal distribution is the best limiting distribution for a parameter that is defined from a finite set of physical measurements (Fornasini, 2008). Based on these settings, we then computed the rating curve and the corresponding propagation of the uncertainty in the stream stage. The spectral expansions introduce the stochasticity of this parameter by using the quadrature node values as a noise value ε. This means that ε increases or reduces the stream stage h_r, for all of the stress periods of the model at each cell that represent the streams. Hence, the stream stages $\hat{h}_r$ used in the deterministic evaluations are defined using a random variable $\varepsilon \sim \mathcal{N}(\mu_\varepsilon, \sigma_\varepsilon)$ to represent the stage error, where $\mu_\varepsilon = 0$, as follows:

$$\hat{h}_r = h_r + \varepsilon. \tag{22}$$

For the definition of prior parameter distributions of the conductance, we consider physically suitable ranges according to the streambed material. In addition, given the lack of prior information related to the conductance properties of the streambed, we assume uniform density distributions to maximize the entropy for both the canal and the river conductance $\mathcal{U}(a, b)$ (Cousquer et al., 2017; Zeng et al., 2016). Table 1b includes the actual values that were applied for the prior distributions.

The magnitude and direction of the flow fields were calculated at the center of the cell by computing the flow face-to-face from the MODFLOW outputs and applying the same semi-analytical algorithm described in a previous section and defined by Pollock (2012). We implemented the polynomial expansions, the nonintrusive pseudo-spectral projection, and the kernel density estimation using the Chaospy library (Feinberg, 2019; Feinberg & Langtangen, 2015) and the SciPy library (Virtanen et al., 2020).

Table 2
Mean Absolute Error (in Meters) of the Expected Values at the Monitoring Wells Using Different Values of Quadrature Degree and qMC Validation With 1,000 Samples

Method	K	n	P	Monitoring well				Average
				Alzpitz	B1	B3	B4	
gPC	2	2	27	0.0971	0.1999	0.1836	0.0952	0.1440
	3	1	64	0.1262	0.1876	0.1590	0.0919	0.1412
	3	3	64	0.1262	0.1876	0.1590	0.0919	0.1412
	4	1	125	0.1165	0.1916	0.1663	0.0926	0.1417
	4	2	125	0.1165	0.1916	0.1663	0.0926	0.1417
	4	4	125	0.1165	0.1916	0.1663	0.0926	0.1417
	5	2	216	0.1187	0.1905	0.1649	0.0925	0.1416
	5	3	216	0.1187	0.1905	0.1649	0.0925	0.1416
	5	5	216	0.1187	0.1905	0.1649	0.0925	0.1416
	6	2	343	0.1184	0.1907	0.1650	0.0925	0.1417
	6	3	343	0.1184	0.1907	0.1650	0.0925	0.1417
	8	3	729	0.1184	0.1907	0.1650	0.0925	0.1417
	9	2	1,000	0.1184	0.1907	0.1650	0.0925	0.1416
	10	4	1,331	0.1184	0.1907	0.1650	0.0925	0.1417
	12	5	2,197	0.1184	0.1907	0.1650	0.0925	0.1417
qMC	–	–	1,000	0.1205	0.1896	0.1628	0.0922	0.1413

The simulated groundwater heads were evaluated in relation to the set of observed values. Also, we validated the results obtained from the gPC method by comparing the simulated groundwater heads with the results from the application of a quasi-Monte Carlo method (qMC) with $S = 1000$ samples. The sampling points for the qMC were generated using Halton sequences (Halton, 1964) as a low-discrepancy arrangement to reduce the variance in the samples and considering that the convergence rate of quasi-random sequences is $\mathcal{O}(\ln N^d / N)$ (Smith, 2013). Further explanations of how the collocation of the uncertain values differs between the methods are provided in Annex A in Supporting Information S1 for illustrative purposes.

3. Results and Discussion

To present some of the results clearly, we extracted them at specific time steps to understand the responses of the system at the following time steps: before the event at stress period 86 (23 May 2013), peak-flow at stress period 127 (02 June 2013), recession phase at stress period 145 (07 June 2013) and after the flood event at stress period 290 (13 July 2013).

We performed various tests to define K and n, which included the application of the empirical rule presented by Sudret (2008), the full factorial design (Smith, 2013; Xiu, 2010), and a series of experimental combinations. We calculated the mean absolute error [L] of the expected values of the groundwater head [L] from the gPC expansions and the qMC sampling [L] in relation to the observed values at the monitoring wells. The results from these evaluations are displayed in Table 2. As mentioned by Debuscherre (2017), in practical applications of the polynomial expansions, the selection of the order of representation of the expansions is an experimental choice that depends on the problem. We observed that low quadrature degrees were able to capture the dependence between the solution and the stochastic spaces. Indeed, the convergence of the results does not significantly improve by using $K > 4$. Consequently, we applied $K = 4$ and $n = 4$ to proceed with the quantification of uncertainty and the creation of probability maps. In addition, to validate this choice against the qMC results, we performed a comparison of the spatial distribution of the statistical moments of the hydraulic heads at different phases of the flood event that can be found in the Annex B in Supporting Information S1.
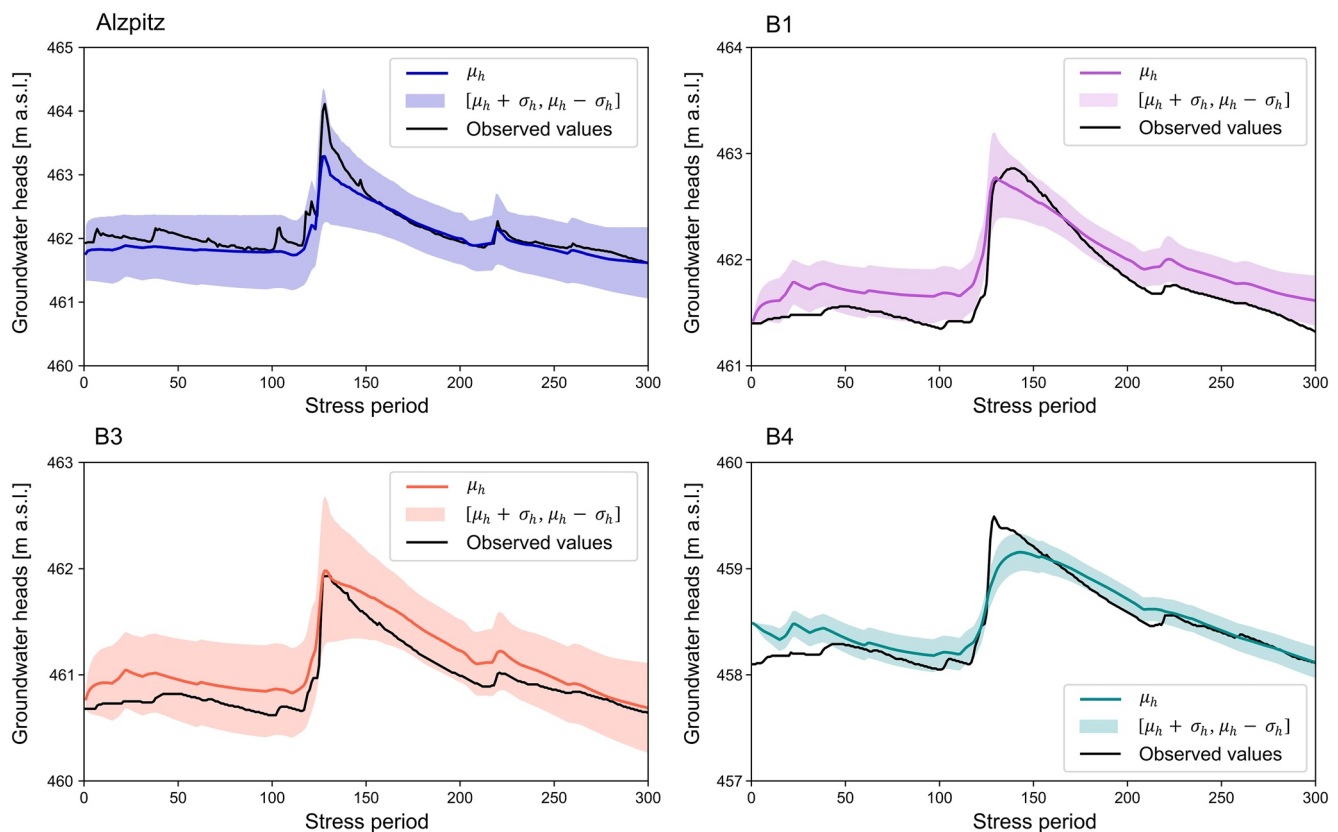
Figure 3. Simulated groundwater heads (colored line), observed values of the groundwater head at the monitoring wells (black line) and uncertainty bounds of the groundwater head (colored shade).

Figure 3 includes the observed groundwater heads and the statistical moments that we obtained using the gPC method along the whole simulation period. The expected value and the standard deviation are represented by μ_h and σ_h, respectively. Notice that the colored shade in the plots represents the interval $[\mu_h + \sigma_h, \mu_h - \sigma_h]$. Overall, the model responses are more accurate in the monitoring wells close to the streams. The expected values at Alzpitz, the closest monitoring well to the streams, represent the observed values properly and mimic the responses of the aquifer during the flood event. The Alzpitz monitoring well is placed in the riverbank and the discrepancies observed between modeled and measured data may be a consequence of the inability of the model to replicate the propagation of the overbank flow on the flood plain. This would lead to the underestimation of the exchange flow at the peak of the event. Similarly, the responses at B3 are well characterized, even though there is a bias in relation to the expected value of the heads. Regarding the uncertainty bounds, we see that the prediction intervals of 1standard deviation cover the ranges of the observed values in the monitoring wells located immediately close to the streams. On the other hand, the results at B1 and B4 are less accurate than the results at Alzpitz and B3 and do not properly match the values of the observations. We attribute these outcomes to inaccuracies in the time-variant specified-head boundary conditions that mainly control the groundwater flow at these points and were extracted from the preexisting regional model (Keilholz et al., 2015). In our research, we primarily relied on the evaluation of Alzpitz and B3, because these are in the vicinity of the streams and the main drivers are the boundary conditions imposed in the canal and the river.

The uncertainty at the peak-flow of the flood event is higher than the uncertainty before the event and at the recession phase (see Table 3). Therefore, despite the fact that the uncertainty in the stream stage has the same statistical distribution over time, the highest uncertainties are observed during the peak-flow event. The deviation for the stage uncertainty was defined

Table 3
Predictive Uncertainty Represented by the Standard Deviation Results (in Meters) at Different Phases of the Flood Event Computed at the Monitoring Wells

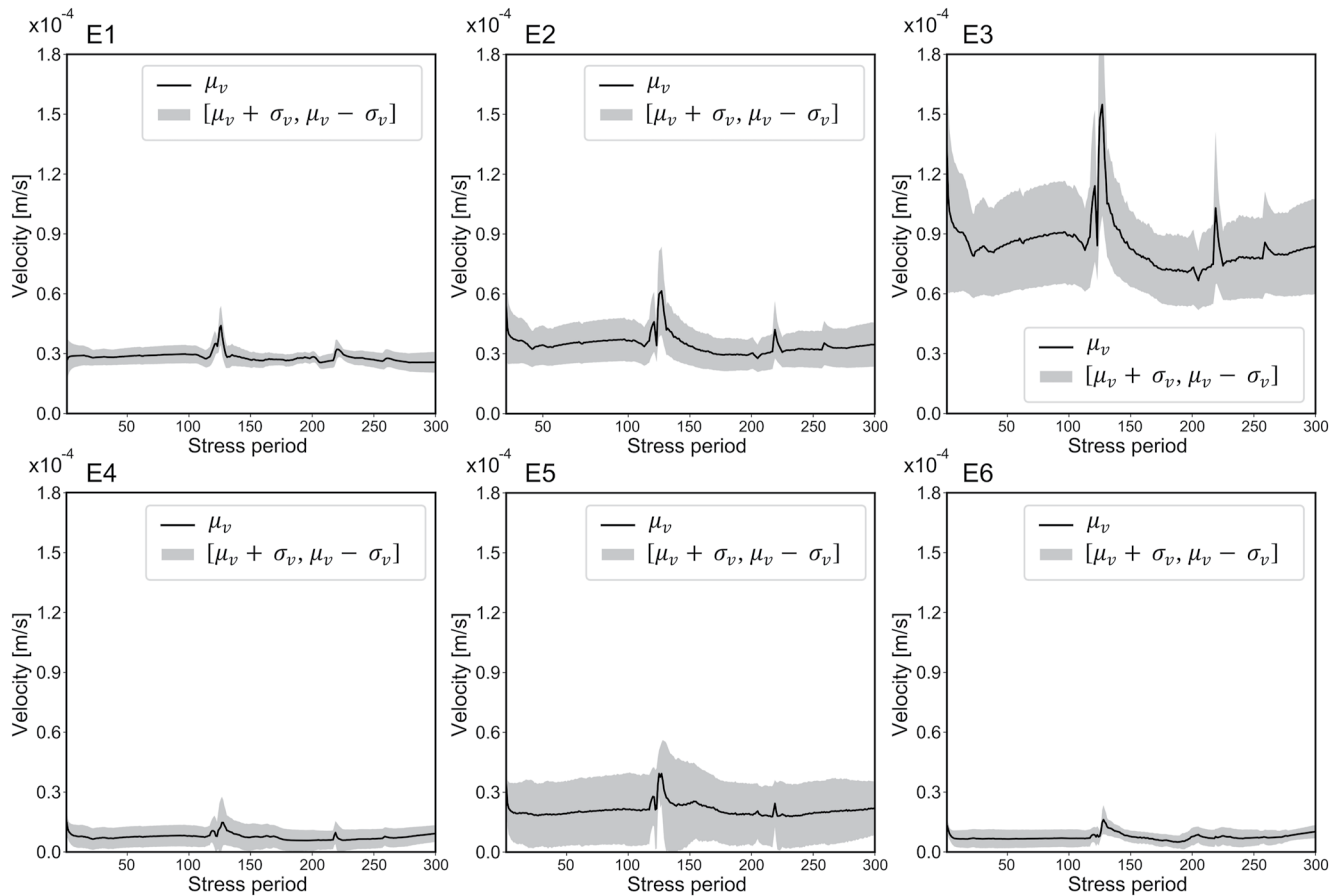| Monitoring well	Before flood (stress period: 86)	Peak-flow (stress period: 127)	Recession phase (stress period: 145)	After flood (stress period: 290)
Alzpitz	0.5744	1.0737	0.5765	0.5326
B1	0.2510	0.4489	0.2548	0.2225
B3	0.4254	0.6987	0.4580	0.4032
B4	0.1522	0.1796	0.1697	0.1420

Figure 4. Simulated expected value of the flow field magnitude (black line) and uncertainty bounds of the flow field (gray shade).

based on the uncertainties calculated by Willems (2011) for high discharge conditions, but not for extreme event conditions. Notice that the uncertainty in discharge and head observation during exceptional flow conditions (e.g., during flood events) can be higher than the uncertainty under ordinary flow conditions (Di Baldassarre & Montanari, 2009).

The propagation of uncertainty in the groundwater flow field was also quantified and the results were extracted at six different points (from E1 to E6), which are shown in Figure 2a. Since the magnitude and direction of the flow fields respond to the hydraulic gradients, the different evaluation points show the behavior of the subsurface system depending on the river and the canal behavior. The high stages in the streams increase the steepness of the gradients and raise the expected value of the velocity μ_v in the vicinity of the streams (see Figure 4). This effect and the large hydraulic conductivity of the gravel and sand in the alluvial plain allow a rapid increase of the magnitude of the flow field. Therefore, it is possible to see the highest average velocities at the peak-flow in all six monitoring points. During the recession phase of the flood, the velocity not only decreases but also the uncertainty, which is represented by the standard deviation σ_v, also drops because of the reduction in the head difference between streams and aquifer at this phase. The highest velocities are registered at E3 due to the hydraulic gradients and the hydraulic conductivity of the alluvial terrace.

As observed in E4 and E5, the velocity and the uncertainty south of the joining streams vary highly at short distances (~40 m between E4 and E5). In this region, the intensity of the signals is controlled by the conductance and the stage of both the canal and the river. The response at E4 may be a consequence of the dominance of the signal coming from the stream stage. Conversely, at E5, rather than one hydraulic pulse, more signals may affect the head variability and the propagated uncertainty in a similar magnitude due to the relative distance of both of the streams and their interaction with the regular groundwater flow regime. As observed, the standard deviation at E3 and E5 are higher than the standard deviation at the other evaluation points.
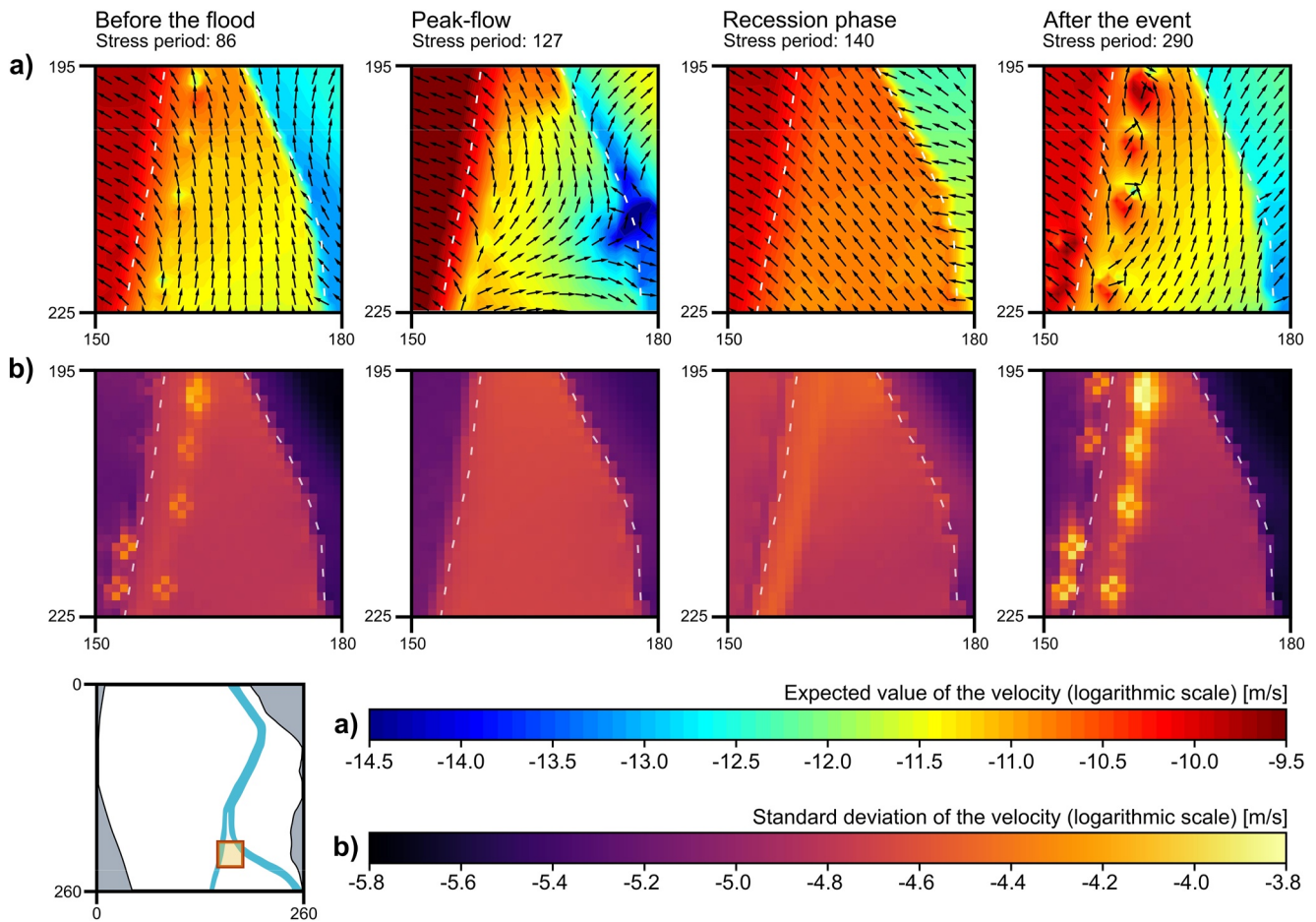
Figure 5. Statistics of the flow field at the river and canal confluence: (a) expected value of the velocity (colored cells) and expected value of the direction (black arrows), and (b) standard deviation of the velocity (colored cells). The river and canal locations are referenced by the white dashed line.

As seen in Figure 4, the results give evidence of a complex dynamic of the groundwater flow in the region where the streams converge. A limitation of our study is certainly the lack of field information from south of the convergence of the streams. This emphasizes the need and significance of quantifying the uncertainty due to surface water and groundwater interaction. To see the behavior south of the junction of the streams in detail, we extracted the results of the flow fields to display the velocity vectors in Figure 5. Figure 5a includes the expected value of the flow fields at the different phases of the flood event, and Figure 5b shows the spatial distribution of the standard deviation of the velocity. Notice that Figures 5a and 5b display the results in a logarithmic scale to facilitate the examination. With the same purpose, the vector arrows in Figure 5a only show the direction of the vector and were upscaled applying an interpolation that queries the nearest cell values.

During the peak-flow, we observed major variations in the magnitude and direction of the flow field. The eastern side of the river shows slow flow due to the convergence of fluxes, while the flow velocity below the canal reaches its maximum. In the recession phase, we can observe a dominant orientation of the flow from southeast to northwest. The magnitude and direction almost recover to the initial state after the flood. In Figure 5b, we observe major uncertainties before and after the event. This may occur because there is not a single signal that independently controls the flow field in the selected domain during this period. Therefore, small changes in the values of the stream parameters may imply significant modifications of the magnitude of the flow field at the meter-scale. Lower values of the standard deviation are found below the streams and also the recession phase is the least uncertain.

The probability density functions of the directions were obtained from the kernel density estimation. In Figure 6, we represent the probability density function of the flow field direction within a two-dimensional polar
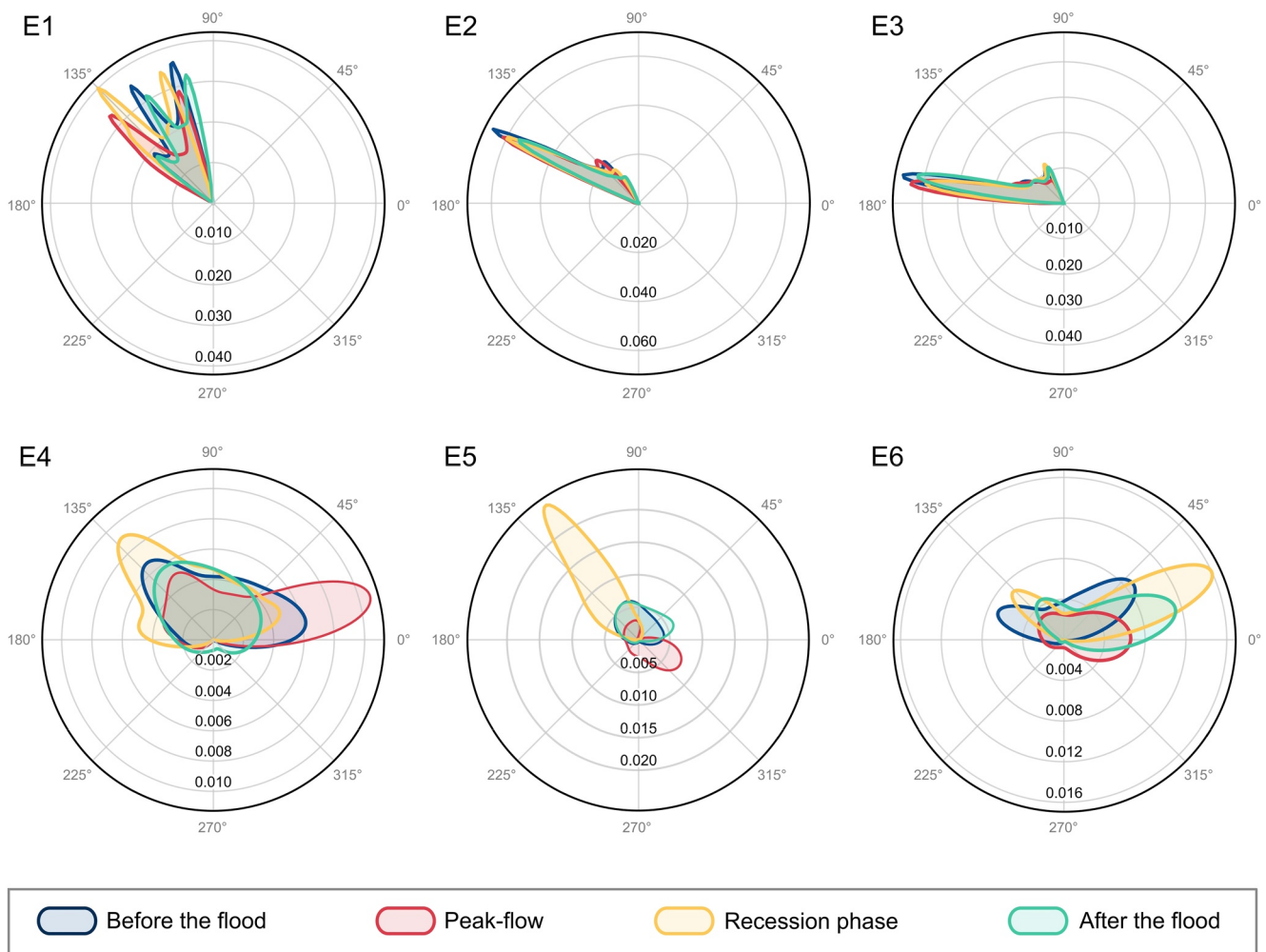
Figure 6. Propagation of uncertainty in the flow field direction. The probability density function of the flow field direction is represented within a two-dimensional polar coordinate system labeled in degrees.

coordinate system labeled in degrees. In this reference system, the direction is defined by the angular coordinate in degrees, and the frequency is represented by the radial coordinate [-] as the distance from the origin. We observed variations in the direction of the flow field at every stage of the flood event. The significance of these variations depends on the spatial location and the underlying geomorphological and hydrological features. The evaluation points located west of the streams (E1, E2, and E3) present small changes in the expected value of the direction. However, the uncertainty is higher at E1 than at E2 and E3. South of the confluence of the streams, the orientations fluctuate considerably. As mentioned above, the flow fields depend on two diverse hydraulic pulses from different sources. One is the river, where the wave propagates without any immediate anthropogenic intervention. The second one is the canal, where the discharge is modulated by the upstream infrastructure. The E4, E5, and E6 evaluation points show major changes in the mean direction at every stage of the flood event. Similarly, the values of the standard deviation are higher, and the uncertainty varies highly at every stage of the event. The highest values of standard deviation of the direction can be observed at the peak of the event, particularly at E1, E4, E5, and E6. At the E5 evaluation point, we observe the most critical change in the orientation of the flow fields. Before the flood, we can observe the usual groundwater flow regime from southeast to northwest. At the peak of the flood event, the expected direction points toward the southeast. Afterward, during the recession of the flood, the flow follows the general reach regime in direction to the northeast. Observing E4 and E5 in Figure 6, and given the morphological conditions of the streams, we may expect to find reverse flow. However, we can also observe that, although the evaluation points are relatively close, the standard deviation and the mean of the direction can change considerably in short distances. This behavior is similar to the one observed in the velocity
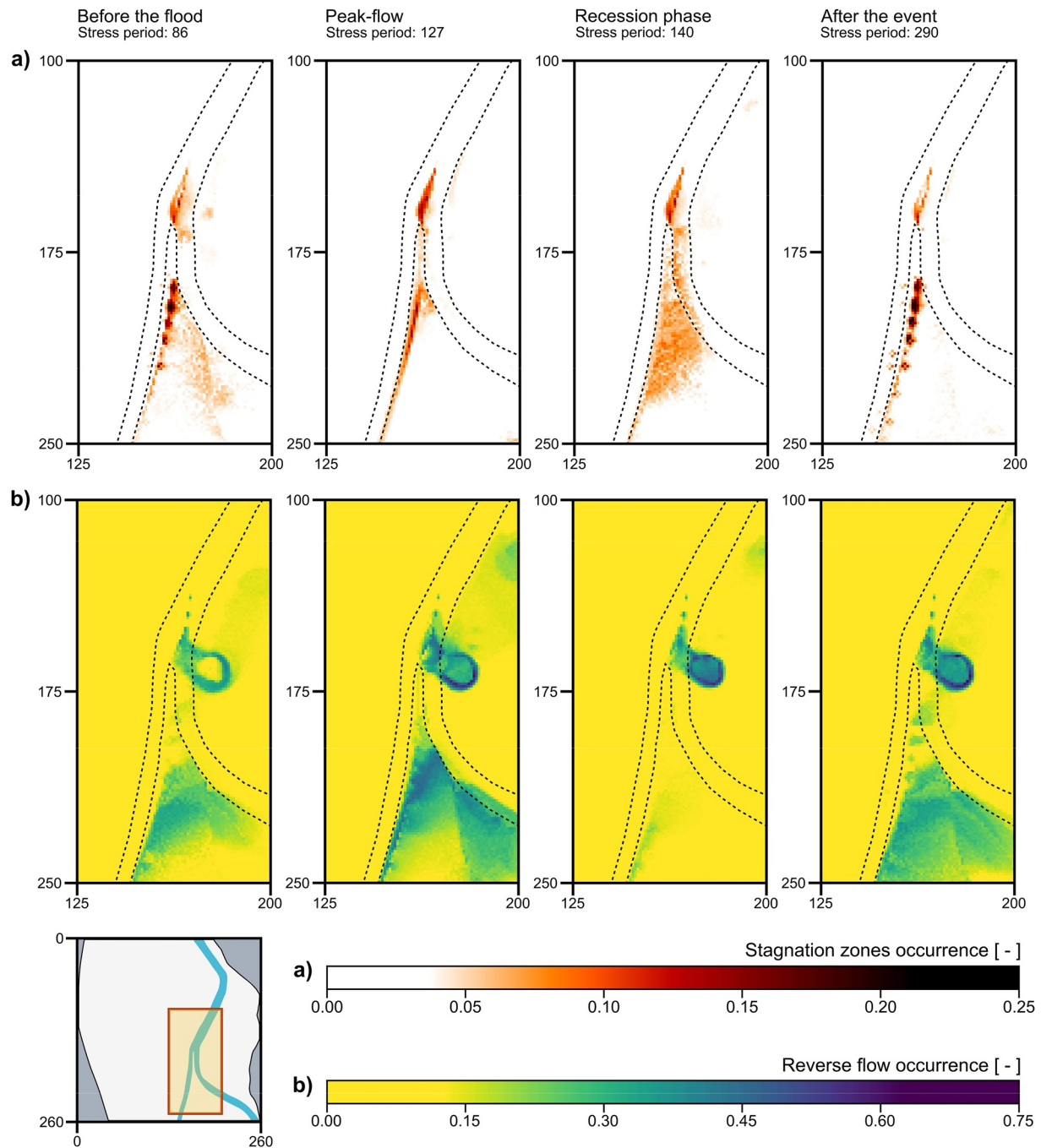
Figure 7. Probability of occurrence of flow features: (a) stagnation zones at different phases of the flood event, and (b) reverse flow at different phases of the flood event. The river and canal locations are referenced by the black dotted line.

calculations. These substantial distinctions underline the need to define the effects of the uncertainties due to river boundary conditions in terms of space and time, particularly considering the limited field observations in this zone.

The probability maps of the stagnation zones are presented in Figure 7a. We can distinguish different spots in space and time with higher sensitivity to the uncertainty in the river boundary conditions. In this case, we observe the probability of finding points where the local velocity is zero. Before and after the flood, we can observe black dots along the canal that show a relatively high probability of occurrence of stagnation points (~25%). This

occurs in the places where different signals from the canal, the river and the aquifer meet. Also, at the junction of the canal and the river, it is possible to observe a stable stagnation region with a probability of occurrence from 10% to 15% for all the phases of the flood. This can occur due to the immediate counterflow that depends on the pressure heads of the streams that could produce the cancellation of the hydraulic pulses. The occurrence of stagnation zones decreases highly during the peak-flow event because of the high hydraulic gradients, which increase the groundwater flow velocities. Nevertheless, at the peak-flow event, one can observe a fringe of a probable stagnation zone along the eastern border of the canal.

The second flow feature that we analyzed is the occurrence of reverse flows. We can observe the extracted results in Figure 7b. The probability of finding reverse flows in the domain dramatically increases during the peak-flow event, reaching a value of ∼75%. One of the reasons for this is the high streambed conductance in the canal, which allows the exchange of flow during maximum discharge. At this phase, we have the highest hydraulic heads of the stage in the canal, which changes the regular hydraulic gradient and produces flows against the regional flow at the meter-scale. During the recession phase, the probability of finding reverse flows drops considerably. At this phase, the flood event starts a contraction defined by an extensive drop of the hydraulic gradients. It is also interesting to observe a spot of constantly high reverse probability allocated east of the junction of the streams. We attribute the high probabilities in this spot to the encounter of the discharges from the river and canal that increases the hydraulic pressure in the aquifer after the confluence of the two water bodies. The mean direction at this zone can be highly affected by the input uncertainty of stream stage and the conductance. Variations in these inputs can change the ordinary south-north flow to a lateral east-west flow due to the degree of flow exchange and can even affect the losing and gaining stream conditions. Regions near the confluence of the streams are prone to the presence of both stagnation points and reverse flow at different phases of the flood event. This area is very dynamic due to the interaction of the streams and the aquifer. Despite the apparent spatial correlation, there is a temporal difference in the responses. At peak-flow, the probability of stagnation zones increases and the probability of reverse flow decreases. In terms of fluid mixing, transport of solutes and temperature fluxes, these zones may play a meaningful role and may be highly affected by the uncertainties in the river boundary conditions. In our opinion, this is evidence of the importance of quantifying the uncertainty in the river boundary conditions and properly representing stream-aquifer interactions in numerical models.

4. Conclusions

In this study, we computed the probability of occurrence of stagnation zones and reverse flow in a numerical model based on the prior uncertainty of the river boundary conditions. The framework consists of the application of gPC expansions solved by a pseudo-spectral approach to obtain point estimates of the statistical information. We subsequently used kernel density estimations to take advantage of the information stored in the probability density functions of the quantities of interest. Finally, the flow fields were assessed according to a series of criteria that allowed us to identify hotspots of stagnation zones and reverse flow. A key feature of this work is the use of these techniques at every single cell of a distributed groundwater model. This allows us to explicitly map the flow field magnitude and direction in terms of statistical moments and the probability of occurrence in terms of spatial distribution and temporal variation.

This approach does not require further work for setting up preexisting models, because the pseudo-spectral approach is a nonintrusive technique, and the solutions are achieved using a relatively low number of model evaluations (125 evaluations in this study). This means that a model can be treated as a black-box solver to calculate the expansion coefficients. This is quite practical considering that groundwater models that include river boundary conditions are often calibrated by tweaking the streambed conductance, which is a model parameter that can vary over time. Additionally, hydrogeological models are usually updated by adding time-variant processes, such as streamflow information and stream stages, for forecasting purposes. At the same time, we find this framework beneficial due to the flexibility to choose the precision and the computational cost. Due to the smooth dependence between the solution and the random spaces, a low quadrature degree may be sufficient to get accurate responses and other quantities of interest can be computed at a low marginal cost. Considering that the deterministic calculation at every element of a distributed model is usually the expensive part of the groundwater numerical simulations, an affordable approach is convenient for constructing spatial maps.

We validate the generalized polynomial chaos expansion as a method for quantifying the uncertainty in a real case study with a model that simulates flood events on surface water-groundwater interaction. The highest posterior uncertainties are found at the peak-flow phase, while the lowest uncertainties are observed at the recession phase of the flood. This occurs despite the fact that we used the same stream stage prior distribution over the whole simulation time to compute the expansion coefficients. The outcomes of this work give evidence of the complex hydrodynamic features occurring during the flood event due to the convergence of separate surface streams and their exchange flow with the aquifer. In consequence, there is significant uncertainty in the flow dynamics at the river boundaries that should be properly quantified. This is reflected in the probability of finding stagnation and reverse flow at the meter and reach scale, despite the groundwater regime flowing predominantly along-valley. We can observe that the regions near the confluence of the streams are very dynamic and prone to exhibit stagnation zones and reverse flow. However, the probabilities of occurrence clearly vary at different phases of the flood event. At the peak-flow, the probability of occurrence of stagnation zones increases, while the probability of occurrence of reverse flow decreases. The major effects on the water flux and the flow paths are transitory and relative to the spatial location and the hydrogeological conditions of the stream-aquifer system. Although the methodology was applied to one specific case study, it can be more broadly stated that flow reversal and stagnation points can appear at the river confluence, where streams and highly permeable aquifers are well connected.

Data Availability Statement

The code infrastructure, the programming scripts, the simulation results, and the database files are stored and available in the online repository: Merchán-Rivera et al. (2021), with license CC BY 4.0. Annex A and B are included in Supporting Information S1.

References

Anderson, M. P., & Munter, J. A. (1981). Seasonal reversals of groundwater flow around lakes and the relevance to stagnation points and lake budgets. *Water Resources Research*, *17*, 1139–1150. https://doi.org/10.1029/WR017i004p01139

Anderson, M. P., Woessner, W. W., & Hunt, R. J. (2015). *Applied groundwater modeling: Simulation of flow and advective transport*. Academic Press.

Arrigoni, A. S., Poole, G. C., Mertes, L. A. K., O'Daniel, S. J., Woessner, W. W., & Thomas, S. A. (2008). Buffered, lagged, or cooled? Disentangling hyporheic influences on temperature cycles in stream channels. *Water Resources Research*, *44*. https://doi.org/10.1029/2007WR006480

Bachmat, Y., & Robert S. Kerr Environmental Research Laboratory, Holcomb Research Institute. (1978). *Utilization of numerical groundwater models for water resource management*. Environmental Protection Agency, Office of Research and Development; Robert S. Kerr Environmental Research Laboratory, Holcomb Research Institute.

Bayerisches Landesamt für Umwelt. (2017). *UmweltAtlas Bayern*.

Bear, J. (1972). *Dynamics of fluids in porous media, Environmental science series (New York, 1972)*. American Elsevier Pub. Co.

Bernard-Jannin, L., Brito, D., Sun, X., Jauch, E., Neves, R., Sauvage, S., & Sánchez-Pérez, J.-M. (2016). Spatially distributed modelling of surface water-groundwater exchanges during overbank flood events – A case study at the Garonne River. *Advances in Water Resources*, *94*, 146–159. https://doi.org/10.1016/j.advwatres.2016.05.008

Beven, K., & Binley, A. (1992). The future of distributed models: Model calibration and uncertainty prediction. *Hydrological Processes*, *6*, 279–298. https://doi.org/10.1002/hyp.3360060305

Bhaskar, A. S., Harvey, J. W., & Henry, E. J. (2012). Resolving hyporheic and groundwater components of streambed water flux using heat as a tracer. *Water Resources Research*, *48*. https://doi.org/10.1029/2011WR011784

Boano, F., Harvey, J. W., Marion, A., Packman, A. I., Revelli, R., Ridolfi, L., & Wörman, A. (2014). Hyporheic flow and transport processes: Mechanisms, models, and biogeochemical implications. *Reviews of Geophysics*, *52*, 603–679. https://doi.org/10.1002/2012RG000417

Boano, F., Revelli, R., & Ridolfi, L. (2013). Modeling hyporheic exchange with unsteady stream discharge and bedform dynamics: Unsteady hyporheic exchange with moving bed forms. *Water Resources Research*, *49*, 4089–4099. https://doi.org/10.1002/wrcr.20322

Bresciani, E., Kang, P. K., & Lee, S. (2019). Theoretical analysis of groundwater flow patterns near stagnation points. *Water Resources Research*, *55*, 1624–1650. https://doi.org/10.1029/2018WR023508

Brunner, P., Simmons, C. T., Cook, P. G., & Therrien, R. (2010). Modeling surface water-groundwater interaction with MODFLOW: Some considerations. *Ground Water*, *48*, 174–180. https://doi.org/10.1111/j.1745-6584.2009.00644.x

Brunner, P., Therrien, R., Renard, P., Simmons, C. T., & Franssen, H.-J. H. (2017). Advances in understanding river-groundwater interactions: River-Groundwater Interactions. *Reviews of Geophysics*, *55*, 818–854. https://doi.org/10.1002/2017RG000556

Cameron, R. H., & Martin, W. T. (1947). The orthogonal development of non-linear functionals in series of Fourier-hermite functionals. *Annals of Mathematics*, *48*, 385. https://doi.org/10.2307/1969178

Cardenas, M. B. (2008). Surface water-groundwater interface geomorphology leads to scaling of residence times. *Geophysical Research Letters*, *35*, L08402. https://doi.org/10.1029/2008GL033753

Cardenas, M. B., & Zlotnik, V. A. (2003). Three-dimensional model of modern channel bend deposits: 3D model of channel bend deposit. *Water Resources Research*, *39*. https://doi.org/10.1029/2002WR001383

Casas-Mulet, R., Alfredsen, K., Hamududu, B., & Timalsina, N. P. (2015). The effects of hydropeaking on hyporheic interactions based on field experiments. *Hydrological Processes*, *29*, 1370–1384. https://doi.org/10.1002/hyp.10264

Chiogna, G., Hochstetler, D. L., Bellin, A., Kitanidis, P. K., & Rolle, M. (2012). Mixing, entropy and reactive solute transport. *Geophysical Research Letters*, *39*, 2012GL053295. https://doi.org/10.1029/2012GL053295

Conant, B., Robinson, C. E., Hinton, M. J., & Russell, H. A. J. (2019). A framework for conceptualizing groundwater-surface water interactions and identifying potential impacts on water quality, water quantity, and ecosystems. *Journal of Hydrology*, *574*, 609–627. https://doi.org/10.1016/j.jhydrol.2019.04.050

Cools, R., & Nuyens, D. (2016). *Monte Carlo and quasi-Monte Carlo methods*.

Cousquer, Y., Pryet, A., Flipo, N., Delbart, C., & Dupuy, A. (2017). Estimating river conductance from prior information to improve surface-subsurface model calibration. *Groundwater*, *55*, 408–418. https://doi.org/10.1111/gwat.12492

Cui, G., Su, X., Liu, Y., & Zheng, S. (2020). Effect of riverbed sediment flushing and clogging on river-water infiltration rate: A case study in the Second Songhua River, Northeast China. *Hydrogeology Journal*, *29*(2), 551–565 https://doi.org/10.1007/s10040-020-02218-7

Debusschere, B. (2017). Intrusive polynomial Chaos methods for forward uncertainty propagation. In Ghanem, R., Higdon, D., & Owhadi, H. (Eds.), *Handbook of uncertainty quantification*. Springer International Publishing. https://doi.org/10.1007/978-3-319-12385-1_19

Deman, G., Konakli, K., Sudret, B., Kerrou, J., Perrochet, P., & Benabderrahmane, H. (2016). Using sparse polynomial chaos expansions for the global sensitivity analysis of groundwater lifetime expectancy in a multi-layered hydrogeological model. *Reliability Engineering & System Safety*, *147*, 156–169. https://doi.org/10.1016/j.ress.2015.11.005

DHI. (2013). *The MIKE SHE user and technical reference manual*. Danish Hydraulic Institute.

Di Baldassarre, G., & Montanari, A. (2009). Uncertainty in river discharge observations: A quantitative analysis. *Hydrology and Earth System Sciences*, *13*, 913–921. https://doi.org/10.5194/hess-13-913-2009

Di Ciacca, A., Leterme, B., Laloy, E., Jacques, D., & Vanderborght, J. (2019). Scale-dependent parameterization of groundwater–surface water interactions in a regional hydrogeological model. *Journal of Hydrology*, *576*, 494–507. https://doi.org/10.1016/j.jhydrol.2019.06.072

Doppler, G., Kroemer, E., Rögner, K., Wallner, J., Jerz, H., & Grottenthaler, W. (2011). *Quaternary stratigraphy of southern Bavaria*. https://doi.org/10.23689/FIDGEO-1763

Dudley-Southern, M., & Binley, A. (2015). Temporal responses of groundwater-surface water exchange to successive storm events. *Water Resources Research*, *51*, 1112–1126. https://doi.org/10.1002/2014WR016623

Elliott, A. H., & Brooks, N. H. (1997). Transfer of nonsorbing solutes to a streambed with bed forms: Laboratory experiments. *Water Resources Research*, *33*, 137–151. https://doi.org/10.1029/96WR02783

Esfandiar, B., Porta, G., Perotto, S., & Guadagnini, A. (2015). Impact of space-time mesh adaptation on solute transport modeling in porous media. *Water Resources Research*, *51*, 1315–1332. https://doi.org/10.1002/2014WR016569

Feinberg, J. (2019). *ChaosPy – Uncertainty Quantification Library [WWW Document]. ChaosPy – Uncertainty Quantification Library*. Retrieved from https://chaospy.readthedocs.io/en/master/

Feinberg, J., & Langtangen, H. P. (2015). Chaospy: An open source tool for designing methods of uncertainty quantification. *Journal of Computational Science*, *11*, 46–57. https://doi.org/10.1016/j.jocs.2015.08.008

Fetter, C. W. (1999). *Contaminant hydrogeology*. Prentice Hall.

Findlay, S. (1995). Importance of surface-subsurface exchange in stream ecosystems: The hyporheic zone. *Limnology & Oceanography*, *40*, 159–164. https://doi.org/10.4319/lo.1995.40.1.0159

Fornasini, P. (2008). *The uncertainty in physical measurements: An introduction to data analysis in the physics laboratory*. Springer.

Francis, B. A., Francis, L. K., & Cardenas, M. B. (2010). Water table dynamics and groundwater-surface water interaction during filling and draining of a large fluvial island due to dam-induced river stage fluctuations. *Water Resources Research*, *46*. https://doi.org/10.1029/2009WR008694

Gautschi, W. (1968). Construction of Gauss-Christoffel quadrature formulas. *Mathematics of Computation*, *22*, 251. https://doi.org/10.1090/S0025-5718-1968-0228171-0

Georgakakos, K. P., Seo, D.-J., Gupta, H., Schaake, J., & Butts, M. B. (2004). Towards the characterization of streamflow simulation uncertainty through multimodel ensembles. *Journal of Hydrology*, *298*, 222–241. https://doi.org/10.1016/j.jhydrol.2004.03.037

Gerecht, K. E., Cardenas, M. B., Guswa, A. J., Sawyer, A. H., Nowinski, J. D., & Swanson, T. E. (2011). Dynamics of hyporheic flow and heat transport across a bed-to-bank continuum in a large regulated river. *Water Resources Research*, *47*. https://doi.org/10.1029/2010WR009794

Ghaith, M., & Li, Z. (2020). Propagation of parameter uncertainty in SWAT: A probabilistic forecasting method based on polynomial chaos expansion and machine learning. *Journal of Hydrology*, *586*, 124854. https://doi.org/10.1016/j.jhydrol.2020.124854

Ghysels, G., Benoit, S., Awol, H., Jensen, E. P., Debele Tolche, A., Anibas, C., & Huysmans, M. (2018). Characterization of meter-scale spatial variability of riverbed hydraulic conductivity in a lowland river (Aa River, Belgium). *Journal of Hydrology*, *559*, 1013–1027. https://doi.org/10.1016/j.jhydrol.2018.03.002

Ghysels, G., Mutua, S., Veliz, G. B., & Huysmans, M. (2019). A modified approach for modelling river–aquifer interaction of gaining rivers in MODFLOW, including riverbed heterogeneity and river bank seepage. *Hydrogeology Journal*, *27*, 1851–1863. https://doi.org/10.1007/s10040-019-01941-0

Gibson, N. L., Gifford-Miears, C., Leon, A. S., & Vasylkivska, V. S. (2014). Efficient computation of unsteady flow in complex river systems with uncertain inputs. *International Journal of Computer Mathematics*, *91*, 781–797. https://doi.org/10.1080/00207160.2013.854336

Golub, G. H., & Welsch, J. H. (1968). Calculation of Gauss quadrature rules. *Mathematics of Computation*, *23*, 221. https://doi.org/10.1090/S0025-5718-69-99647-1

Gomez, J. D., & Wilson, J. L. (2013). Age distributions and dynamically changing hydrologic systems: Exploring topography-driven flow: Age distributions for hydrologic systems. *Water Resources Research*, *49*, 1503–1522. https://doi.org/10.1002/wrcr.20127

Götzinger, J., & Bárdossy, A. (2008). Generic error model for calibration and uncertainty estimation of hydrological models. *Water Resources Research*, *44*. https://doi.org/10.1029/2007WR006691

Halton, J. H. (1964). Algorithm 247: Radical-inverse quasi-random point sequence. *Communications of the ACM*, *7*, 701–702. https://doi.org/10.1145/355588.365104

Harbaugh, A. (2005). MODFLOW-2005, The U.S. Geological Survey Modular Ground-Water Model—The Ground-Water Flow Process. In U.S. Geological Survey Techniques and Methods 6-A16. U.S. Geological Survey.

Hatch, C. E., Fisher, A. T., Ruehl, C. R., & Stemler, G. (2010). Spatial and temporal variations in streambed hydraulic conductivity quantified with time-series thermal methods. *Journal of Hydrology*, *389*, 276–288. https://doi.org/10.1016/j.jhydrol.2010.05.046

Hidalgo, J. J., & Dentz, M. (2018). Mixing across fluid interfaces compressed by convective flow in porous media. *Journal of Fluid Mechanics*, *838*, 105–128. https://doi.org/10.1017/jfm.2017.888

Hidalgo, J. J., Dentz, M., Cabeza, Y., & Carrera, J. (2015). Dissolution patterns and mixing dynamics in unstable reactive flow. *Geophysical Research Letters*, *42*, 6357–6364. https://doi.org/10.1002/2015GL065036

Hubbs, S. A. (2006). Evaluating streambed forces impacting the capacity of riverbed filtration systems. In Hubbs, S. A. (Ed.), *Riverbank filtration hydrology, Nato science series: IV: Earth and environmental sciences*. Springer. https://doi.org/10.1007/978-1-4020-3938-6_2

Hunt, R. J., Strand, M., & Walker, J. F. (2006). Measuring groundwater–surface water interaction and its effect on wetland stream benthic productivity, Trout Lake watershed, northern Wisconsin, USA. *Journal of Hydrology*, *320*, 370–384. https://doi.org/10.1016/j.jhydrol.2005.07.029

Jiang, X.-W., Wan, L., Wang, J.-Z., Yin, B.-X., Fu, W.-X., & Lin, C.-H. (2014). Field identification of groundwater flow systems and hydraulic traps in drainage basins using a geophysical method: Jiang et al.: Identification of flow systems. *Geophysical Research Letters*, *41*, 2812–2819. https://doi.org/10.1002/2014GL059579

Jiang, X.-W., Wang, X.-S., Wan, L., & Ge, S. (2011). An analytical study on stagnation points in nested flow systems in basins with depth-decaying hydraulic conductivity. *Water Resources Research*, *47*. https://doi.org/10.1029/2010WR009346

Jones, J. B., & Holmes, R. M. (1996). Surface-subsurface interactions in stream ecosystems. *Trends in Ecology & Evolution*, *11*, 239–242. https://doi.org/10.1016/0169-5347(96)10013-6

Keilholz, P., Disse, M., & Bhola, P. (2015). Integrierte Betrachtung der Grundhochwasser-Problematik in der Gemeinde Tacherting (Bayern). *Hydrologie und Wasserbewirtschaftung*, 688–693. https://doi.org/10.3243/kwe2015.11.003

Krause, S., Boano, F., Cuthbert, M. O., Fleckenstein, J. H., & Lewandowski, J. (2014). Understanding process dynamics at aquifer-surface water interfaces: An introduction to the special section on new modeling approaches and novel experimental technologies: Introduction. *Water Resources Research 50*, 1847–1855. https://doi.org/10.1002/2013WR014755

Krause, S., Lewandowski, J., Grimm, N. B., Hannah, D. M., Pinay, G., McDonald, K., et al. (2017). Ecohydrological interfaces as hot spots of ecosystem processes. *Water Resources Research 53*, 6359–6376. https://doi.org/10.1002/2016WR019516

Kuczera, G., & Mroczkowski, M. (1998). Assessment of hydrologic parameter uncertainty and the worth of multiresponse data. *Water Resources Research*, *34*, 1481–1489. https://doi.org/10.1029/98WR00496

Laloy, E., Rogiers, B., Vrugt, J. A., Mallants, D., Jacques, D. (2013). Efficient posterior exploration of a high-dimensional groundwater model from two-stage Markov chain Monte Carlo simulation and polynomial chaos expansion: Speeding up MCMC Simulation of a Groundwater Model. *Water Resources Research 49*, 2664–2682. https://doi.org/10.1002/wrcr.20226

Le Gratiet, L., Marelli, S., & Sudret, B. (2017). Metamodel-based sensitivity analysis: Polynomial Chaos expansions and Gaussian processes. In Ghanem, R., Higdon, D., & Owhadi, H. (Eds.), *Handbook of uncertainty quantification*. Springer International Publishing. https://doi.org/10.1007/978-3-319-12385-1_38

Le Maitre, O. P., & Knio, O. M. (2010). *Spectral methods for uncertainty quantification: With applications to computational fluid dynamics, Scientific computation*. Springer.

Lewandowski, J., Arnon, S., Banks, E., Batelaan, O., Betterle, A., Broecker, T., et al. (2019). Is the hyporheic zone relevant beyond the scientific community? *Water*, *11*, 2230. https://doi.org/10.3390/w11112230

Lewandowski, J., Meinikmann, K., & Krause, S. (2020). Groundwater–surface water interactions: Recent advances and interdisciplinary challenges. *Water*, *12*, 296. https://doi.org/10.3390/w12010296

Litvinenko, A., Logashenko, D., Tempone, R., Wittum, G., & Keyes, D. (2020). Solution of the 3D density-driven groundwater flow problem with uncertain porosity and permeability. *International Journal on Geomathematics*, *11*, 10. https://doi.org/10.1007/s13137-020-0147-1

Magliozzi, C., Grabowski, R. C., Packman, A. I., & Krause, S. (2018). Toward a conceptual framework of hyporheic exchange across spatial scales. *Hydrology and Earth System Sciences*, *22*, 6163–6185. https://doi.org/10.5194/hess-22-6163-2018

Maina, F. Z., & Guadagnini, A. (2018). Uncertainty quantification and global sensitivity analysis of subsurface flow parameters to gravimetric variations during pumping tests in unconfined aquifers. *Water Resources Research*, *54*, 501–518. https://doi.org/10.1002/2017WR021655

Malzone, J. M., Lowry, C. S., & Ward, A. S. (2016). Response of the hyporheic zone to transient groundwater fluctuations on the annual and storm event time scales: Transient model of the hyporheic zone. *Water Resources Research*, *52*, 5301–5321. https://doi.org/10.1002/2015WR018056

Marzadri, A., Tonina, D., & Bellin, A. (2013). Effects of stream morphodynamics on hyporheic zone thermal regime: Stream morphology control on hyporheic temperature. *Water Resources Research*, *49*, 2287–2302. https://doi.org/10.1002/wrcr.20199

Mehl, S., & Hill, M. C. (2010). Grid-size dependence of Cauchy boundary conditions used to simulate stream–aquifer interactions. *Advances in Water Resources*, *33*, 430–442. https://doi.org/10.1016/j.advwatres.2010.01.008

Meng, J., & Li, H. (2017). An efficient stochastic approach for flow in porous media via sparse polynomial chaos expansion constructed by feature selection. *Advances in Water Resources*, *105*, 13–28. https://doi.org/10.1016/j.advwatres.2017.04.019

Merchán-Rivera, P., Chiogna, G., Disse, M., & Bhola, P. (2018). Surface water and groundwater interaction during flood events in the Alz Valley: Numerical modeling and solute transport simulations. In *Interacción de Agua Superficial y Agua Subterránea. Hidrogeología de Salares. XIV Congreso Latinoamericano de Hidrogeología*. Editorial de la Universidad Nacional de Salta.

Merchán-Rivera, P., Wohlmuth, B, & Chiogna, G. (2021). Dataset and algorithms for identifying stagnation zones and reverse flow caused by river-aquifer interaction. Mendeley Data, V2. https://doi.org/10.17632/mvtd4fjjvj.2

Morel-Seytoux, H. J. (2019). MODFLOW's River Package: Part 1: A Critique. PSIJ 1–9. https://doi.org/10.9734/psij/2019/v22i230129

Morel-Seytoux, H. J., Miller, C. D., Miracapillo, C., & Mehl, S. (2017). River seepage conductance in large-scale regional studies. *Groundwater*, *55*, 399–407. https://doi.org/10.1111/gwat.12491

Oladyshkin, S., de Barros, F. P. J., & Nowak, W. (2012). Global sensitivity analysis: A flexible and efficient framework with an example from stochastic hydrogeology. *Advances in Water Resources*, *37*, 10–22. https://doi.org/10.1016/j.advwatres.2011.11.001

Osman, K. T. (2013). *Forest soils: Properties and management*. Springer International Publishing. https://doi.org/10.1007/978-3-319-02541-4

Peyrard, D., Sauvage, S., Vervier, P., Sanchez-Perez, J. M., & Quintard, M. (2008). A coupled vertically integrated model to describe lateral exchanges between surface and subsurface in large alluvial floodplains with a fully penetrating river. *Hydrological Processes*, *22*, 4257–4273. https://doi.org/10.1002/hyp.7035

Pinay, G., Peiffer, S., De Dreuzy, J.-R., Krause, S., Hannah, D. M., Fleckenstein, J. H., et al. (2015). Upscaling nitrogen removal capacity from local hotspots to low stream orders' drainage basins. *Ecosystems*, *18*, 1101–1120. https://doi.org/10.1007/s10021-015-9878-5

Pollock, D. W. (2012). User Guide for MODPATH version 6—A Particle-Tracking model for MODFLOW, Open-File Report, U.S. Geological Survey Techniques and Methods 6–A41. The Survey; U.S. Geological Survey, Earth Science Information Center [distributor]. https://doi.org/10.3133/ofr94464

Rajabi, M. M. (2019). Review and comparison of two meta-model-based uncertainty propagation analysis methods in groundwater applications: Polynomial chaos expansion and Gaussian process emulation. *Stochastic Environmental Research and Risk Assessment*, *33*, 607–631. https://doi.org/10.1007/s00477-018-1637-7

Rajabi, M. M., & Ataie-Ashtiani, B. (2016). Efficient fuzzy Bayesian inference algorithms for incorporating expert knowledge in parameter estimation. *Journal of Hydrology*, *536*, 255–272. https://doi.org/10.1016/j.jhydrol.2016.02.029

Rajabi, M. M., Ataie-Ashtiani, B., & Simmons, C. T. (2015). Polynomial chaos expansions for uncertainty propagation and moment independent sensitivity analysis of seawater intrusion simulations. *Journal of Hydrology*, *520*, 101–122. https://doi.org/10.1016/j.jhydrol.2014.11.020

Reddy, P. J. R. (2005). *A text book of hydrology*. Laxmi Publications.

Ren, J., & Zhao, B. (2020). Model-based analysis of the effects of rippled bed morphologies on hyporheic exchange. *Journal of Hydrologic Engineering*, *25*, 04020023. https://doi.org/10.1061/(ASCE)HE.1943-5584.0001931

Scott, D. W. (2014). *Multivariate density estimation: Theory, practice, and visualization*. Wiley.

Silverman, B. W. (1998). *Density estimation for statistics and data analysis, Monographs on statistics and applied probability*. Chapman & Hall/CRC.

Singh, T., Gomez-Velez, J. D., Wu, L., Wörman, A., Hannah, D. M., & Krause, S. (2020). Effects of successive peak-flow events on hyporheic exchange and residence times. *Water Resources Research*. https://doi.org/10.1029/2020WR027113

Smith, R. C. (2013). *Uncertainty quantification: Theory, implementation, and applications, computational science and engineering*. SIAM.

Sochala, P., & Le Maître, O. P. (2013). Polynomial Chaos expansion for subsurface flows with uncertain soil parameters. *Advances in Water Resources*, *62*, 139–154. https://doi.org/10.1016/j.advwatres.2013.10.003

Stanford, J. A., & Ward, J. V. (1988). The hyporheic habitat of river ecosystems. *Nature*, *335*, 64–66. https://doi.org/10.1038/335064a0

Stewardson, M. J., Datry, T., Lamouroux, N., Pella, H., Thommeret, N., Valette, L., & Grant, S. B. (2016). Variation in reach-scale hydraulic conductivity of streambeds. *Geomorphology*, *259*, 70–80. https://doi.org/10.1016/j.geomorph.2016.02.001

Sudret, B. (2008). Global sensitivity analysis using polynomial chaos expansions. *Reliability Engineering & System Safety*, *93*, 964–979. https://doi.org/10.1016/j.ress.2007.04.002

Sund, N. L., Bolster, D., Dawson, C. (2015). Upscaling transport of a reacting solute through a periodically converging–diverging channel at pre-asymptotic times. *Journal of Contaminant Hydrology*, *182*, 1–15. https://doi.org/10.1016/j.jconhyd.2015.08.003

Tóth, J. (1963). A theoretical analysis of groundwater flow in small drainage basins. *Journal of Geophysical Research*, *68*, 4795–4812. https://doi.org/10.1029/JZ068i016p04795

Trauth, N., & Fleckenstein, J. H. (2017). Single discharge events increase reactive efficiency of the hyporheic zone. *Water Resources Research*, *53*, 779–798. https://doi.org/10.1002/2016WR019488

Virtanen, P., Gommers, R., Oliphant, T. E., Haberland, M., Reddy, T., Cournapeau, D., et al. (2020). SciPy 1.0: Fundamental algorithms for scientific computing in Python. *Nature Methods*, *17*, 261–272. https://doi.org/10.1038/s41592-019-0686-2

Vrugt, J. A., Gupta, H. V., Bouten, W., Sorooshian, S. (2003). A Shuffled Complex Evolution Metropolis algorithm for optimization and uncertainty assessment of hydrologic model parameters. *Water Resources Research*, *39*. https://doi.org/10.1029/2002WR001642

Wand, M. P., & Jones, M. C. (1995). Kernel smoothing. In *Monographs on statistics and applied probability*. Chapman & Hall.

Wang, X.-S., Wan, L., Jiang, X.-W., Li, H., Zhou, Y., Wang, J., & Ji, X. (2017). Identifying three-dimensional nested groundwater flow systems in a Tóthian basin. *Advances in Water Resources*, *108*, 139–156. https://doi.org/10.1016/j.advwatres.2017.07.016

Willems, W. (2011). *Unsicherheit von Wasserstands- und Abflussmessungen an A-Pegeln des Landes Bayern, Auftragsstudie für das Bayerische Landesamt für Umwelt*. LfU Bayern.

Willems, W., & Stricker, K. (2012). *Bewertung der Qualität von Abflusszeitreihendaten anhand eines mathematisch/statistisch ermittelten Unsicherheitskriteriums, Auftragsstudie für das Bayerische Landesamt für Umwelt*. LfU Bayern.

Winter, T. C. (1976). *Numerical simulation analysis of the interaction of lakes and ground water (USGS Numbered Series No. 1001), Numerical simulation analysis of the interaction of lakes and ground water*. Professional Paper. U.S. Government Printing Office. https://doi.org/10.3133/pp1001

Winter, T. C. (1998). *Ground water and surface water: A single resource, U.S. Geological Survey circular*. U.S. Geological Survey.

Winter, T. C. (1999). Relation of streams, lakes, and wetlands to groundwater flow systems. *Hydrogeology Journal 7*, 28–45. https://doi.org/10.1007/s100400050178

Woessner, W. W. (2000). Stream and fluvial plain ground water interactions: Rescaling hydrogeologic thought. *Ground Water 38*, 423–429. https://doi.org/10.1111/j.1745-6584.2000.tb00228.x

Wu, L., Singh, T., Gomez-Velez, J., Nützmann, G., Wörman, A., Krause, S., & Lewandowski, J. (2018). Impact of dynamically changing discharge on hyporheic exchange processes under gaining and losing groundwater conditions. *Water Resources Research*, *54*. https://doi.org/10.1029/2018WR023185

Xiu, D. (2007). Efficient collocational approach for parametric uncertainty analysis. *Communications in Computational Physics* 293–309.

Xiu, D. (2009). *Fast numerical methods for stochastic computations: A review*.

Xiu, D. (2010). *Numerical methods for stochastic computations: A spectral method approach*. Princeton University Press.

Xiu, D., & Karniadakis, G. E. (2002). The Wiener-Askey polynomial chaos for stochastic differential equations. *SIAM Journal on Scientific Computing*, *24*, 619–644. https://doi.org/10.1137/S1064827501387826

Zeng, X., Wu, J., Wang, D., Zhu, X., & Long, Y. (2016). Assessing Bayesian model averaging uncertainty of groundwater modeling based on information entropy method. *Journal of Hydrology*, *538*, 689–704. https://doi.org/10.1016/j.jhydrol.2016.04.038

Zhang, D., & Lu, Z. (2004). An efficient, high-order perturbation approach for flow in random porous media via Karhunen–Loève and polynomial expansions. *Journal of Computational Physics*, *194*, 773–794. https://doi.org/10.1016/j.jcp.2003.09.015

Zhang, P., DeVries, S. L., Dathe, A., & Bagtzoglou, A. C. (2009). Enhanced mixing and plume containment in porous media under time-dependent oscillatory flow. *Environmental Science & Technology*, *43*, 6283–6288. https://doi.org/10.1021/es900854r